RSC Advances

PAPER

View Article Online
View Journal | View Issue

Cite this: *RSC Adv.*, 2023, **13**, 24211

Localized surface plasmon resonance shift of biosynthesized and functionalized quasi-spherical gold nanoparticle systems†

Ricky Kristan M. Raguindin * and Candy C. Mercado

Rapid and more environment-friendly means of gold nanoparticle synthesis is necessary in many applications, as in ion detection. Leaf extracts have become effective and economical reducing agents for gold nanoparticle formation, however, effects of extract combinations have not been thoroughly investigated. With the exploitation of combined extract effects, gold nanoparticles were synthesized then functionalized and investigated to produce selected nanoparticle systems which are capable of detecting aqueous lead(II) ions with minimum detection limits of 10–11 ppm. The measured localized surface plasmon resonance absorption peaks of the gold nanoparticles were 541–800 nm for the synthesis and 549 nm for the functionalization. The diameters of different gold nanoparticle systems were 17–37 nm. These were mostly quasi-spherical in morphology with some rod-, triangular-, and hexagonal plate-like particles. The biosynthesis used polyphenols and acids present in the extracts in the reduction of gold ions into gold nanoparticles, and in the nanoparticle capping and stabilization. Functionalization replaced the capping compounds with alliin, *S*-allylcysteine, allicin, and ajoene. Gold nanoparticle stability in aqueous systems was verified for two weeks up to five months. The investigations concluded the practicability of the gold nanoparticles in lead(II) ion detection with selectivity initially verified for other divalent cations.

Received 18th June 2023
Accepted 8th August 2023

DOI: 10.1039/d3ra04092e

rsc.li/rsc-advances

Introduction

Gold (Au) nanoparticles—having promising viability for technological advancements in a multitude of fields such as in optoelectronics, sensing, biomedicine, and nanoelectronics due to their tuneable and morphology-dependent properties—are of great significance to scientific research.[1] With the wide range of possibilities that this material can offer, it is imperative to provide and explore more ways of synthesizing or processing Au nanoparticles especially using natural compounds which pose negligible harm to our health and environment.

In the past years, researchers made use of environment-friendly biosynthesis routes of creating Au nanoparticles. Biosynthesis is the use of biological media, such as plants or bacteria *etc.*, in order to create chemicals or materials. Plants, termed as the 'chemical factories' of nature, and their extracts seem to be a promising option for nanoparticle synthesis because of their cost efficiency and low maintenance aside from the fact that they generally produce nanoparticles with good stability and appropriate dimensions due to a single-step fabrication process.[2] Generally, leaf extracts are also capable of producing Au nanoparticles at room temperature, hence energy-saving benefits add up to their significance.

However, there are still research gaps regarding the effects of extract combination in Au nanoparticle synthesis. In this study, the combinatory extract type effects on the Au nanoparticles were investigated. For the functionalization, a common practice for previous studies is to use specific compounds;[3–5] meanwhile, this study utilized *Allium sativum* (AS) extract with various sulfur (S) containing compounds to highlight the strong Au–S bond. The target application for the synthesis is making the spectroscopically silent lead(II) ion (Pb^{2+}) be detectable in the visible light region for monitoring purposes in aqueous systems.

Lead is toxic which can damage respiratory, cardiovascular, urinary, neurological, and cognitive functions of the human body by means of oxidative, immune-modulation, and inflammatory mechanisms.[6] One of the ways that Pb^{2+} enters the body is through the digestive system which occurs when we eat or drink lead-contaminated food and liquids. The absorption rate of Pb^{2+} from drinking water is 35–50% for adults, while it goes beyond 50% for children.[7] The action level, the point wherein further actions must be implemented, of the United States Environmental Protection Agency (US EPA) for Pb^{2+} in water directed to public drinking water systems is 15 parts per billion (ppb) or 15 $\mu g\ L^{-1}$, but their maximum contaminant level goal is zero since even trace amounts can be detrimental.[8,9] Meanwhile,

---

Department of Mining, Metallurgical and Materials Engineering, College of Engineering, University of the Philippines Diliman, Quezon City 1101, Philippines. E-mail: rmraguindin1@up.edu.ph

† Electronic supplementary information (ESI) available. See DOI: https://doi.org/10.1039/d3ra04092e

the recommended maximum concentration of Pb^{2+} in irrigation water by Ayers and Westcot (1985) is 5 ppm.[10] This value was used as basis of Farid *et al.* (2015)[11] in assessing environmental waters such as canal, ground, and waste water samples. For the National Oceanic and Atmospheric Administration (NOAA), the indicated concentration of Pb^{2+} as the severe effect level is 250 ppm.[12]

Rigorous assessments of water bodies and sources must be carried out for the presence of Pb^{2+}. Inductively coupled plasma mass spectrometry (ICP-MS), atomic absorption spectroscopy (AAS) and inductively coupled plasma optical emission spectrometry (ICP-OES), are some of the techniques used, with high accuracy and advanced instrumentation requiring operation expertise.[13–16] The use of the localized surface plasmon resonance (LSPR) property of Au nanoparticles for intermediate concentration levels is a useful, easy and economical alternative. This can be done by functionalizing or capping the surface of Au nanoparticles with compounds that will interact with varying Pb^{2+} concentrations. According to studies, there is aggregation of gallic acid stabilized Au nanoparticles upon exposure to Pb^{2+}.[17,18] The resulting Au nanoparticles capped with the carboxylic acid functional group (–COOH), more especially with gallic acid, is seen to detect Pb^{2+}. *Lagerstroemia speciosa* (LS) and *Moringa oleifera* (MO) leaf extracts both contain gallic acid,[19,20] and some major compounds of aqueous *Muntingia calabura* (MC) leaf extract are citric and gallic acids.[21] Moreover, a major AS clove compound that contain the S element is alliin or *S*-allyl-l-cysteine sulfoxide[22] which can also be exploited for its affinity to Au (due to the Au–S bond) and Pb^{2+} (due to the –COOH). The Pb^{2+}-induced aggregation of functionalized Au nanoparticles causes a redshift in their LSPR which can provide a correlation with the Pb^{2+} concentration.

Experimental

Preparation of aqueous extracts

Extraction of MC, LS, and MO leaves. The leaves were rinsed with distilled water in order to remove the impurities on their surfaces. Then, they were air-dried without direct sunlight at room temperature for 6–8 days to remove moisture. The air-dried leaves were stored in airtight glass containers prior to grinding them into particles and flakes using a blender. One gram each of the processed leaves were digested *via* a water bath maintained at 84 °C for 45 minutes. The solid–liquid extraction mixtures of each leaf type were cooled to room temperature and filtered using cellulose filter papers (pore size: 5–10 μm). The extracts were indicated by the labels MC (*Muntingia calabura*), LS (*Lagerstroemia speciosa*), and MO (*Moringa oleifera*). Combinations of leaf extracts were made (Table S1†) in preparation for the reaction with chloroauric acid ($HAuCl_4$). All of the remaining extracts were stored in a refrigerator at about 4 °C for future use.

Heat-treatment and extraction of AS cloves. Raw *Allium sativum* cloves were skinned, rinsed with distilled water, dried and sealed in a glass jar, and heated for 30 minutes in 100 °C boiling water, then cooled. The heating procedure limited the conversion of alliin to allicin and other organosulfur compounds by the inactivation of alliinase enzyme.[23] The cloves were combined with water (1 : 1 w/v ratio) then crushed and allowed to stand for an additional 30 minutes at room temperature. Finally, the *Allium sativum* cloves aqueous extract (designated sample code: AS) was filtered and stored at 4 °C for further use.

Au nanoparticle biosynthesis using various leaf extract combinations

The combined leaf extracts, as reducing agents, were added to 5 mM $HAuCl_4$ at room temperature with rapid swirling. The initial time of conversion, based on brown to purple color change, was recorded for each of the systems. The colloids were incubated in dark conditions overnight at about 4 °C to allow complete conversion. The formation of Au nanoparticles was confirmed by the appearance of absorbance peaks due to plasmon resonance. The colloids were centrifuged at 15 200 rpm for 30 minutes then rinsed and dispersed in ultrapure water with short ultrasonication. The Au nanoparticles in ultrapure water were stored at 4 °C. The four resulting colloidal Au nanoparticle systems are indicated in Table 1.

Functionalization of Au-MCLS-1 nanoparticles using AS extract

The Au-MCLS-1 nanoparticle system, synthesized with equal parts of MCLS extract and $HAuCl_4$, was chosen as the initial combination for the functionalization with AS extract. First, Au-MCLS-1 was centrifuged at 15 200 rpm for 30 minutes followed by rinsing and redispersion with ultrapure water. The redispersed nanoparticles were ultrasonicated for 30–60 s. The entire process was repeated three times before AS extract (1 g AS/mL H_2O) was used as the dispersion medium for the nanoparticles. The colloidal system was stored for 68 hours at 4 °C in order to allow the substitution of capping agents by organosulfur compounds. Finally, another cycle of centrifugation-rinsing-redispersion was done to remove the excess AS extract, and ultrapure water was reintroduced as the colloidal dispersion medium. The AS-functionalized Au nanoparticle sample was designated as Au-AS-1 and stored at 4 °C.

Stability assessments

All of the biosynthesized and functionalized Au nanoparticle systems (Au-MCLS-1, Au-LSMO-1, Au-MCMO-1, Au-MLM-1, and Au-AS-1) were immersed in ultrapure water over a period of two weeks to test the stability. From each of the diluted stock colloidal dispersions of Au nanoparticle systems, absorbance spectra of samples were collected. The remaining stock

Table 1 Biosynthesized Au nanoparticles using various combination leaf extracts

Combined extracts	Extract-to-$HAuCl_4$ ratio	Designated sample code
MCLS	1 : 1	Au-MCLS-1
LSMO	1 : 1	Au-LSMO-1
MCMO	1 : 1	Au-MCMO-1
MLM	1 : 1	Au-MLM-1

colloidal dispersions were stored at about 4 °C in the dark. After two weeks, another set of the diluted Au nanoparticle systems were analyzed in which the generated spectra were compared to their initial spectra. The zeta potential values of the Au nanoparticles were measured *via* dynamic light scattering (Malvern Zetasizer Nano ZSP) at 25.0 °C after five months in the storage conditions mentioned.

Lead detection experiments and determination of detection limits

The detection experiments were done for both Au-MCLS-1 and Au-AS-1 nanoparticle systems by comparing the absorbance spectra after exposure to an analyte. The analytes were blank (ultrapure water) and solutions with different Pb^{2+} concentrations (95, 189, 284, 378, 473, 568, 662, 757, and 851 μM). In each test vial, equal amounts of the Au nanoparticle system and analyte were combined, then the absorbance spectrum was taken; the peak wavelength *versus* Pb^{2+} concentration was plotted and the upper and lower limits of Pb^{2+} detection were determined.

Characterization of extracts and Au nanoparticles

Absorbance spectroscopy. The absorbance spectra in the visible light region of Au nanoparticles dispersed in ultrapure water (Au-MCLS-1, Au-LSMO-1, Au-MCMO-1, Au-MLM-1, and Au-AS-1), with a dilution factor of 12, were examined using a UV-vis spectrophotometer (Shimadzu UV-2600i). Spectral shifts and absorbance differences of the Au nanoparticles were accounted for and related to their morphology. Absorbance spectroscopy was also used to compare Au-MCLS-1 and Au-AS-1 for describing the occurrence of functionalization *via* substitution of capping compounds.

^{1}H nuclear magnetic resonance spectroscopy. Au nanoparticles were investigated *via* ^{1}H NMR analysis to identify the compounds responsible for the reduction of Au ions, and the capping or stabilizing and functionalizing of the Au nanoparticles. The solvent used for the systems (Au-MCLS-1, Au-LSMO-1, Au-MCMO-1, Au-MLM-1, and Au-AS-1) was deuterium oxide (D_2O). The analyses were done using Varian 500 MHz (3 mm TRP pfg probe).

Fourier-transform infrared spectroscopy. Transmission mode FTIR analysis using the KBr pellet method was performed as a complement for ^{1}H NMR in order to identify and confirm the capping agents of Au-MCLS-1, Au-LSMO-1, Au-MCMO-1, Au-MLM-1, and Au-AS-1 nanoparticle systems. The Au nanoparticles were dehydrated by air-drying at room temperature for a couple of days prior to the analysis using the FTIR spectrophotometer (Thermo Fisher Nicolet IS50).

Electron microscopy. SEM (Scanning Electron Microcopy) images of the Au nanoparticles (Au-MCLS-1, Au-LSMO-1, Au-MCMO-1, and Au-MLM-1) were taken in order to identify their morphology in a dehydrated state. A droplet of each of the nanoparticle systems was placed on a pre-cleaned and pre-cut silicon wafer, then allowed to dry at room temperature. The dried samples were observed under the Hitachi SU8230 field-emission scanning electron microscope at 50 000–150 000× magnifications with an accelerating voltage of 5.0 kV. ImageJ software was used to obtain the particle sizes. Au-AS-1 nanoparticles were imaged and analyzed using TEM (Transmission Electron Microscopy) with SAED (Selected Area Electron Diffraction) (JEOL JEM-2100F). The Au nanoparticles were deposited in such a way that a drop of the colloidal Au sample was placed on a TEM grid (Ted Pella Carbon Type-B, 200 mesh, Copper with an approximate grid hole size of 97 μm) and then allowed to air-dry prior to the TEM analysis.

Table 2 Summary of ^{1}H NMR peak commonality of the biosynthesized Au nanoparticle systems using different leaf extract combinations[a]

^{1}H NMR spectral range / Au NP system	8.24–8.23 Aromatic-H	5.03 Alkene-H	4.27–4.26 H bonded to a cyclic structure or H bonded to C (bonded to another R group) of a cyclic structure	3.45–3.42 H bonded to C (with OH) of a cyclic alcohol structure	3.33–3.30 Methoxy ($O-CH_3$) or H bonded to C (with OH) of a cyclic alcohol structure	3.15–3.13 H bonded to C (with OH) of a cyclic alcohol structure or H bonded to a junction of cyclic structures	2.02 H bonded to a junction of cyclic structures	0.98–0.94 Methyl ($R-CH_3$)	-0.12 – -0.16 Due to aromatic ring-current effects	-0.79 – -0.80 Due to aromatic ring-current effects
Au-MCLS-1	8.23	5.03	4.26	3.45, 3.44	3.33, 3.31	3.15	2.02	0.98, 0.97, 0.95	-0.15	-0.80
Au-LSMO-1	■	■	■	3.44, 3.42	3.30	■	■	0.97, 0.95, 0.94	-0.12	■
Au-MCMO-1	8.23	■	■	3.44, 3.43	3.30	3.13	■	0.96	-0.16	-0.79
Au-MLM-1	8.24	■	4.27	3.44	3.32	■	■	0.98	■	-0.79

[a] Black regions indicate absence of peaks per Au nanoparticle system.

Results and discussion

Effects of leaf extract combinations on Au nanoparticles

Nanoparticle formation and LSPR. Combined leaf extracts reduced Au ions into Au nanoparticles wherein the initial conversion was signaled by a sharp color change from amber to purple.[24] The times of color change were recorded and compared among different extract combinations (presented in Fig. S1 and S2†). Au-MCLS-1 nanoparticle system appeared pinkish purple after 9 seconds of reacting MCLS extract with $HAuCl_4$. A similar, less intense, color change, was observed in the formation of Au-LSMO-1 after 68 seconds. For Au-MCMO-1, the colloidal color was violet which was apparent after 389 seconds. The violet color became more pronounced after the next 120 seconds. A different shade of violet, which has a pinkish tone, was observed after 45 seconds of reacting MLM extract with $HAuCl_4$ in order to produce Au-MLM-1. The color intensity increased for 8 seconds after the onset of color change. Among these four Au nanoparticle systems, Au-MCLS-1 recorded the least time for initial Au formation, while Au-MCMO-1 took the longest time.

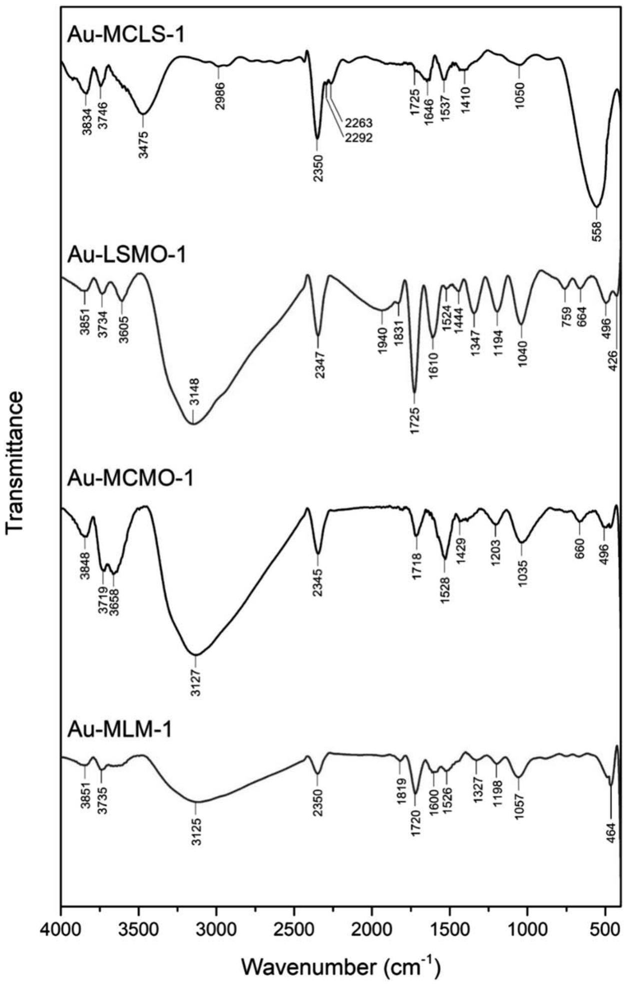

Fig. 1 Functional groups as represented by FTIR spectral peaks of biosynthesized Au nanoparticle systems using various combined leaf extracts (Au-MCLS-1, Au-LSMO-1, Au-MCMO-1, and Au-MLM-1). The corresponding functional groups are detailed in the ESI:† participating biochemical compounds and Table S2.†

Absorbance spectra of the Au nanoparticle systems are shown in Fig. S3.† The spectra of the extracts do not overlap with Au nanoparticle peaks. The LSPR peak of Au-MCLS-1 is at 541 nm. There are two peaks for Au-LSMO-1 which are at 543.75 and 730 nm. Meanwhile, Au-MCMO-1 exhibited a peak at 548.75 nm and Au-MLM-1 at 541.75 nm. It is important taking into consideration that Au-MLM-1 also showed a second less intense peak near the 800 nm wavelength mark. The major peaks correspond to quasi-spherical nanoparticles, while the secondary peaks for Au-LSMO-1 and Au-MLM-1 were attributed to the nanoparticles of different shapes. The order of Au nanoparticles based on LSPR peak wavelength is Au-MCMO-1 > Au-LSMO-1 > Au-MLM-1 > Au-MCLS-1. The LSPR bands as determined by absorbance spectroscopy can also provide information regarding the size of nanoparticles. Increasing sizes of nanoparticles lead to redshifting of the LSPR.[25]

Participating Biochemical Compounds. The ^1H NMR spectra of Au-MCLS-1, AU-LSMO-1, Au-MCMO-1, and Au-MLM-1 are presented in Fig. S4.† Au-MCLS-1 exhibited peaks corresponding to hydrogen atoms bonded to an aromatic group, to an alkene, to a cyclic structure or carbon bonded to another group in a cyclic structure, to a carbon attached to OH of a cyclic alcohol structure, and to a junction of a cyclic structure.[26,27] Moreover, peaks due to hydrogen atoms from methoxy and methyl structures were also found. For Au-LSMO-1, fewer peaks were generated which correspond to hydrogen attached to carbon which is bonded to OH– of a cyclic alcohol structure, hydrogen from methoxy structures, and hydrogen from methyl groups. Au-MCMO-1 has peaks attributed to hydrogen atoms bonded to an aromatic group, to a junction of a cyclic structure, and to a carbon bonded with OH of a cyclic alcohol structure, and hydrogen atoms belonging to methoxy and methyl groups. For Au-MLM-1, the observed peaks represent hydrogen atoms bonded to an aromatic group, to a cyclic structure or carbon bonded to another R group in a cyclic structure, and to a carbon attached to OH of a cyclic alcohol structure, and hydrogen atoms in a methoxy and methyl structures.

Comparisons among the ^1H NMR peaks of Au-MCLS-1, AU-LSMO-1, Au-MCMO-1, and Au-MLM-1 are summarized in Table 2. The peaks present in all of the Au nanoparticle systems that were biosynthesized using varying combination leaf extracts are those corresponding to hydrogens attached to a carbon bonded with OH of a cyclic alcohol structure, and hydrogen atoms belonging to methoxy and methyl groups. The peak for hydrogen attached to an aromatic group was observed in all of the Au nanoparticle systems except for Au-LSMO-1. Only Au-MCLS-1 and Au-MCMO-1 have peaks which could possibly correspond to hydrogen atoms attached to a junction of a cyclic structure. Moreover, Au-MCLS-1 was the sole Au nanoparticle system to exhibit a peak that is attributed to hydrogen bonded to an alkene group. For the peak which could be probably designated to the hydrogen attached to a carbon atom bonded to another R group of a cyclic structure, only Au-MCLS-1 and Au-MLM-1 were able to display such.

To complement the ^1H NMR analysis, FTIR spectroscopy was also done to the Au nanoparticle systems that were biosynthesized using different combinations of leaf extracts. FTIR spectra of Au-MCLS-1, Au-LSMO-1, Au-MCMO-1, and Au-MLM-1 are shown in Fig. 1. Important FTIR peaks were

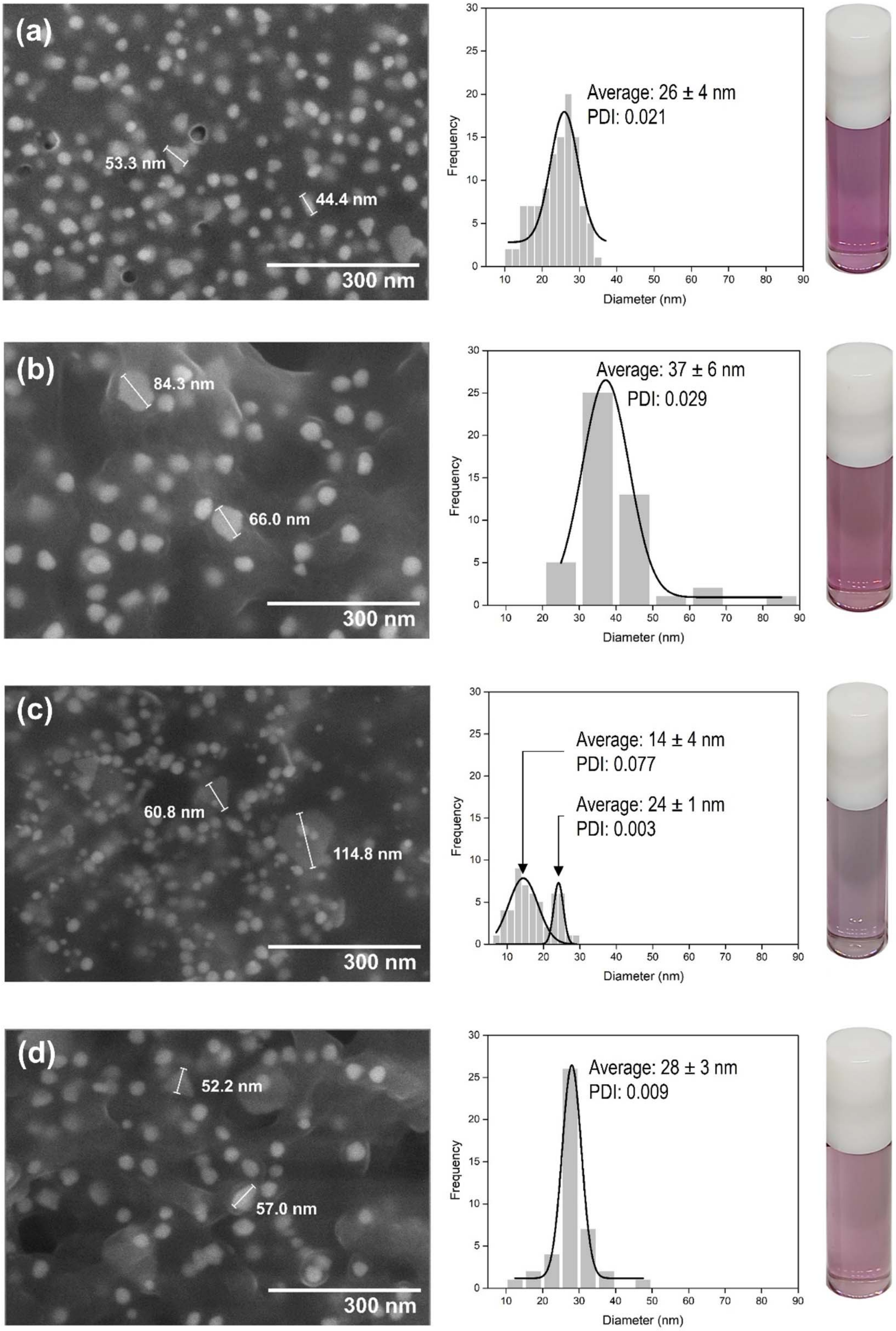

Fig. 2 SEM image analysis of biosynthesized Au nanoparticle systems using various combined leaf extracts: (a) Au-MCLS-1; (b) Au-LSMO-1; (c) Au-MCMO-1, and (d) Au-MLM-1. Except for Au-MCMO-1, all other systems can be considered as monodipersed. The vials contain the Au nanoparticles dispersed in ultrapure water.

attributed to certain functional groups which provide information regarding the capping compounds of the Au nanoparticles.

The comparison of the summaries of functional groups for the Au nanoparticle systems are shown in Table S2.† The recorded ^{1}H NMR and FTIR spectral peaks could be tentatively attributed to various polyphenols and organic acids such as: gallic acid, citric acid, and flavonoid glycosides from MC;[21] caffeic acid, *p*-coumaric acid, corosolic acid, gallic acid, 4-hydroxybenzoic acid, kaempferol, ellagic acid, quercetin, 3-*O*-methylprotocatechuic acid, and isoquercitrin from LS,[28] and chlorogenic acid, gallic acid, and caffeic acid from MO.[29]

Nanoparticle size and stability. In general, the Au colloidal systems produced *via* different combinations of leaf extracts

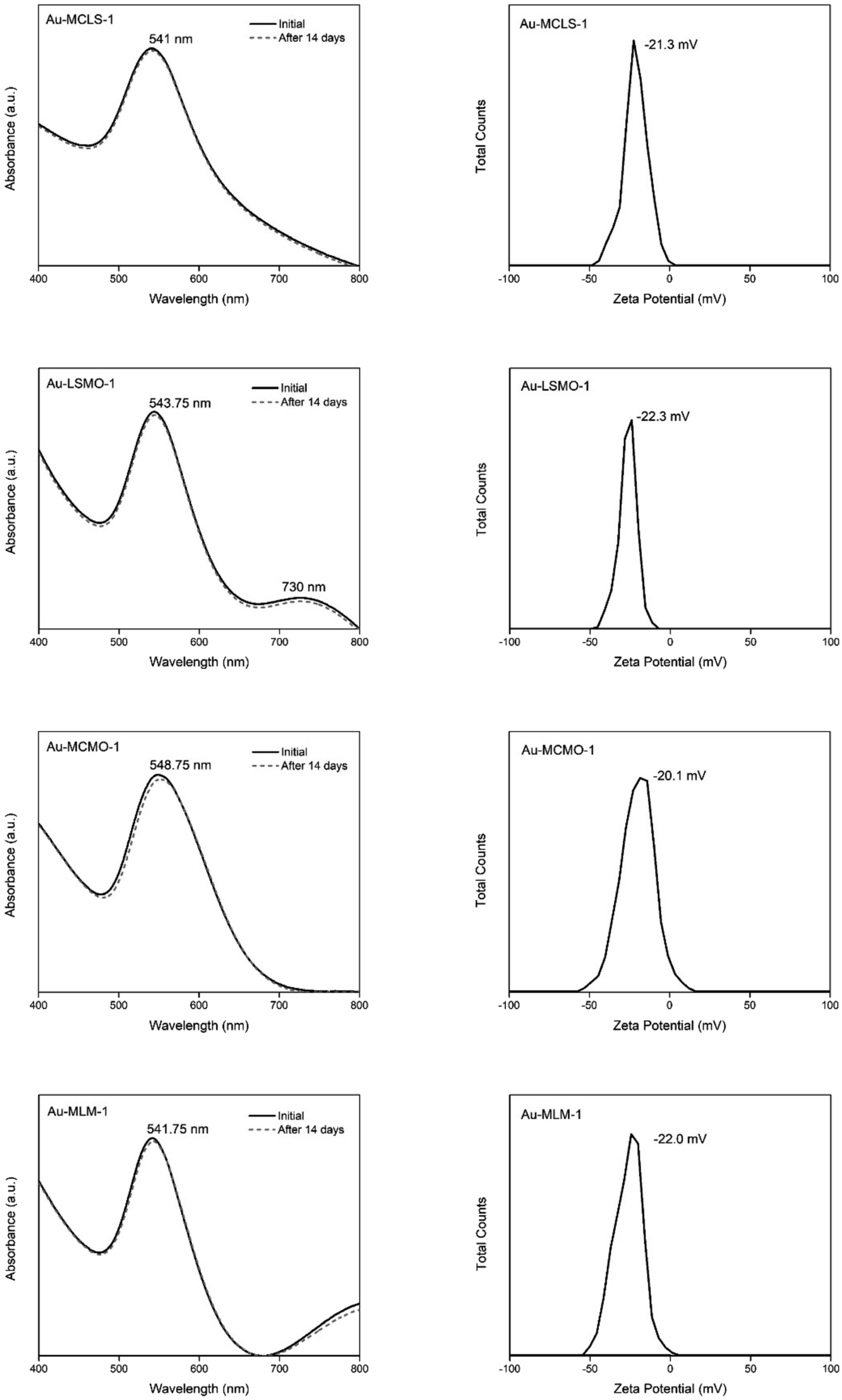

Fig. 3 Analysis of the stability by absorbance spectral comparison and zeta potential of the biosynthesized Au nanoparticle systems using various combination of leaf extracts. All the synthesized nanoparticle systems can be considered stable.

have quasi-spherical as the dominant shape of nanoparticles as shown in Fig. 2. Irregularities in the spherical structure have also been seen – quasi-spherical nanoparticles are prominent in Au-LSMO-1 due to their relatively larger size. Aside from these, few particles are triangular-, hexagonal-, or rod-shaped. The triangular-shaped nanoparticles were distinguishable in Au-MCLS-1, Au-MCMO-1, and Au-MLM-1 nanoparticle systems. Rod-shaped nanoparticles were observed in Au-MCLS-1 and Au-MLM-1. Meanwhile, Au-MCMO-1 exhibited few nanoparticles with hexagonal shape. The hexagonal- and triangular-shaped nanoparticles appear as plate-like structures. The diameter of the particles were taken by ImageJ processing of SEM images to determine their average particle sizes and polydispersity indices. It is important to note that only quasi-spherical nanoparticles were considered in the analyses. Au-MCLS-1, Au-LSMO-1, and Au-MLM-1 showed single-peak Gaussian distribution, while Au-MCMO-1 exhibited a bimodal distribution. Table S3† presents the estimated average quasi-spherical Au nanoparticle size and polydispersity index *via* Gaussian fitting of histograms from SEM Analysis (Fig. 2) using the Origin software. Except for Au-MCMO-1 which has a bimodal distribution, all other three Au nanoparticle systems were monodispersed if quasi-spherical nanoparticles were to be considered. The mean differences of measured quasi-spherical Au nanoparticle sizes from SEM analysis among biosynthesized samples with different combination extracts are all statistically significant. The order of decreasing quasi-spherical nanoparticle size is Au-LSMO-1 > Au-MLM-1 > Au-MCLS-1 > Au-MCMO-1.

The stability of Au-MCLS-1, Au-LSMO-1, Au-MCMO-1, and Au-MLM-1 nanoparticle systems was determined from LSPR spectrum evolution with time (Fig. 3). The Au nanoparticle systems did not exhibit significant changes on their spectra after two weeks. Based on this, the stability of all the Au nanoparticle systems were considered to withstand two weeks without apparent colloidal aggregation. Additionally, the measured zeta potential values of Au-MCLS-1, Au-LSMO-1, Au-MCMO-1, and Au-MLM-1 after five months were −21.3, −22.3, −20.1, and −22.0 mV, respectively and are comparable.

The Au nanoparticles can still be considered as stable after five months based on their zeta potential values. The zeta potential provides information regarding the electrochemical equilibrium at the interface of the liquid medium and Au nanoparticles. Higher magnitudes indicate higher resistance of the particles to aggregation, hence better colloidal stability. For the intended application of Au nanoparticles in this study, good stability of particles prior to ion exposure is beneficial since the mechanism of detection is *via* ion-induced particle attractions. Moreover, the Au nanoparticles exhibited a negative charge while dispersed in an aqueous medium. The negative charge makes the interparticle attractions after cation exposure possible.

The stability is attributed to the capping compounds, such as oxidized polyphenols and organic acids, of the Au nanoparticle systems which also acted as stabilizing agents. Polyphenolic compounds can act as both reducing and stabilizing agents, thus there is no need to introduce other capping agents.[30]

Proposed mechanism of Au nanoparticle biosynthesis. The different combination leaf extracts contain numerous interacting biochemical compounds.[31,32] These compounds include polyphenols and other organic acids which may exist in various structure forms based on their number of carboxylic, phenolic, cyclic and/or aromatic compounds per molecule. They majorly act as the reducing agents of Au ions when the Au solution is allowed to react with the combination of leaf extracts. As Au ion reduction occurs, oxidation of active biochemical compounds (*i.e.* polyphenols and organic acids) also proceeds. Their structures and interactions can affect the final size and shape of Au nanoparticles. Three compounds that reduced Au ions, each having a carboxylate group, could rearrange and nucleate reduced Au atoms to form triangular-shaped nanoparticles. Similarly, three previously-polyphenol compounds that reduced Au ions, each currently having at least two adjacent carbonyl groups bonded to an aromatic group, can arrange themselves to nucleate the reduced Au atoms into hexagonal-shaped nanoparticles. Gallic acid, a type of phenolic acid found in the leaves of the studied plants[21,28,29] is capable of producing spherical Au nanoparticles.[33] The phenolic groups of gallic acid can reduce Au ions, then rearrange with other oxidized gallic acid as if to form a spherical orientation. The orientation involves the carboxylate groups directing the nucleation and growth of the nanoparticles, as well as their capping. Meanwhile, the unoxidized phenolic group of a gallic acid molecule could create a hydrogen bond to one of the oxidized phenolic groups of a neighboring oxidized gallic acid. The hydrogen bonds could also contribute to the strengthening of the overall makeup of a capped nanoparticle, in addition to the Au nanoparticle-to-oxidized group affinity. By following the stated approach, the quasi-spherical Au nanoparticles could be theorized as the result of the combination rearrangements of various oxidized polyphenols and organic acids. The mechanism illustration is presented in Fig. 4.

Rationale of selecting Au-MCLS-1 for further investigations. The Au-MCLS-1 nanoparticle system was chosen because it required the least time to form, it has the smallest average size with good monodispersity, it could have the largest possible detection range since it has the leftmost single absorbance peak, and it has the highest amounts of spherical to quasi-spherical particles with respect to other shapes. It was theorized that Au-MCLS-1, among the other three biosynthesized Au nanoparticle systems, would be the most suitable for ion detection.

Functionalization viability from Au-MCLS-1 to Au-AS-1

LSPR comparison. The color comparison of the AS extract, Au-MCLS-1 and Au-AS-1 is shown in Fig. 5 (inset). The previously pinkish purple Au-MCLS-1 transformed into a violet Au-AS-1. Absorbance spectroscopy showed the difference in the LSPR peak of both Au-MCLS-1 and Au-AS-1. From the 541 nm peak of Au-MCLS-1, an 8 nm redshift was recorded after conversion to Au-AS-1, which had a peak at the 549 nm wavelength as presented in Fig. 5. The LSPR peak shift could be attributed to the displacement or substitution of Au-MCLS-1

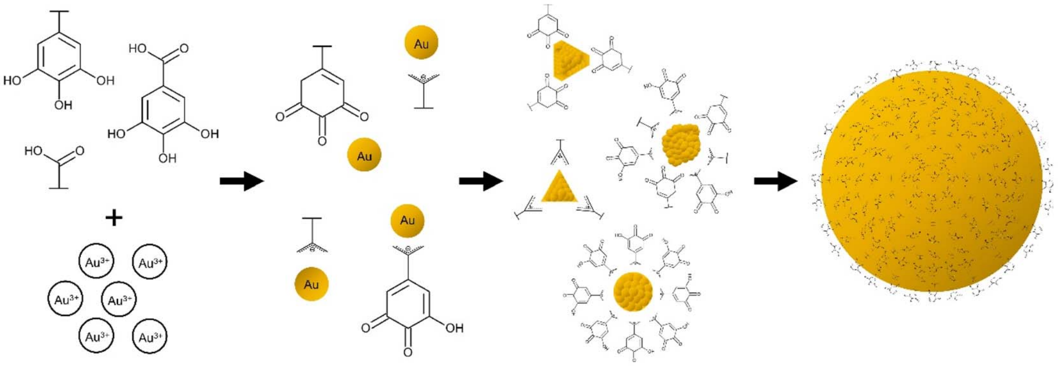

Fig. 4 Graphical representation of proposed biosynthesis and capping mechanism of Au nanoparticles by polyphenols and organic acids. Polyphenols and organic acids can act in the reduction and growth of the biosynthesis of Au nanoparticles in which their interactions can dictate the morphology of the resulting nanoparticles.

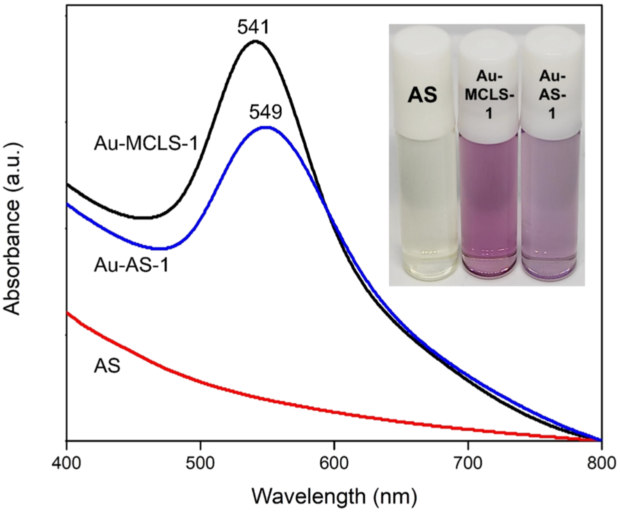

Fig. 5 Comparisons of color and absorbance spectra of AS extract, and the Au nanoparticle systems before (Au-MCLS-1) and after (Au-AS-1) functionalization. A red shift after functionalization signals the substitution of previous capping compounds by AS organosulfur compounds.

capping compounds (*i.e.* oxidized polyphenols and/or organic acids) by organosulfur compounds from AS extract. Moreover, there was a recorded decrease in absorbance from Au-MCLS-1 to Au-AS-1. This LSPR band tends to be very sensitive to the surroundings of the Au nanoparticles such that modifications around the Au core could lead to changes in band intensity and wavelength.[34] In this case, the band changes were due to the alteration in chemical environment of the Au core.

Displacement of biochemical compounds. The Au-AS-1 nanoparticle system ^{1}H NMR spectroscopy generated spectrum interpretations is shown in Fig. 6a while the full-range spectrum is presented in Fig. S5.† In the heat-treatment used for the processing of AS cloves from the study of Imai *et al.* (1994), the resulting extract contained alliin (14.8–16.7 mg g^{-1}), *S*-allylcysteine (0.09–0.11 mg g^{-1}), allicin (0.02–0.03 mg g^{-1}), and ajoene (<0.01 mg g^{-1}).[23] Since the AS extract was used to functionalize Au-MCLS-1 and transform into Au-AS-1, ^{1}H NMR analysis attempted to determine what compounds from AS extract would have affinity to Au nanoparticles. This was confirmed upon the analysis of the Au-MCLS-1 spectrum. ^{1}H NMR spectral features were designated to organosulfur compounds such as alliin, *S*-allylcysteine, (*E*)-ajoene, (*Z*)-ajoene, and allicin. Alliin and *S*-allylcysteine, having quite similar hydrogen atoms in their structures, were considered to have similar peak features in ^{1}H NMR and were based on the research of Jayathilaka *et al.* (2014).[35]. (*E*)-ajoene and (*Z*)-ajoene, being isomers, were also considered to have similar peak features in ^{1}H NMR which were based on the research of Debouzy *et al.* (1989).[36] For allicin, the basis of peak assignments were the researches of Small *et al.* (1947)[37] and Roseblade *et al.* (2017).[38] The spectrum of Au-AS-1 was labeled based on the peak features corresponding to the aforementioned organosulfur compounds. Those peaks with solid-lined boxes were designated to be due to hydrogen atoms from alliin and *S*-allylcysteine, while the solid-lined boxes with asterisk were assigned to the protons of allicin. Moreover, those peaks with broken-lined boxes were designated to be peak features of ajoene, which can either be or both (*E*)-ajoene and (*Z*)-ajoene. The peaks from 5.21 to 5.37 ppm were tentatively attributed to any of the mentioned organosulfur compounds since these peaks seem to be common peak features among them. Peaks from 1.04 to 1.72 ppm were attributed to protons belonging to alkyl CH, while those from 2.15 to 2.63 ppm were assigned to protons of H–C–N or H–C–S structures. Similarities with the ^{1}H NMR peaks among the organosulfur compounds were apparent in the spectrum of Au-AS-1, though there are some features which are more specific to certain types of compounds. The stated compounds could still be subjected for further confirmation. For now, since certain peak features belonging to the stated organosulfur compounds were present in the spectrum, it can be considered that the affinity of Au nanoparticles to the major organosulfur compounds of AS extract is significant.

For comparisons, the ^{1}H NMR spectra for Au-MCLS-1 is presented as inset in Fig. 6. The most intense Au-MCLS-1 peak at 8.23 ppm that was attributed to hydrogen atoms bonded to an aromatic group was also apparently missing in the spectra of

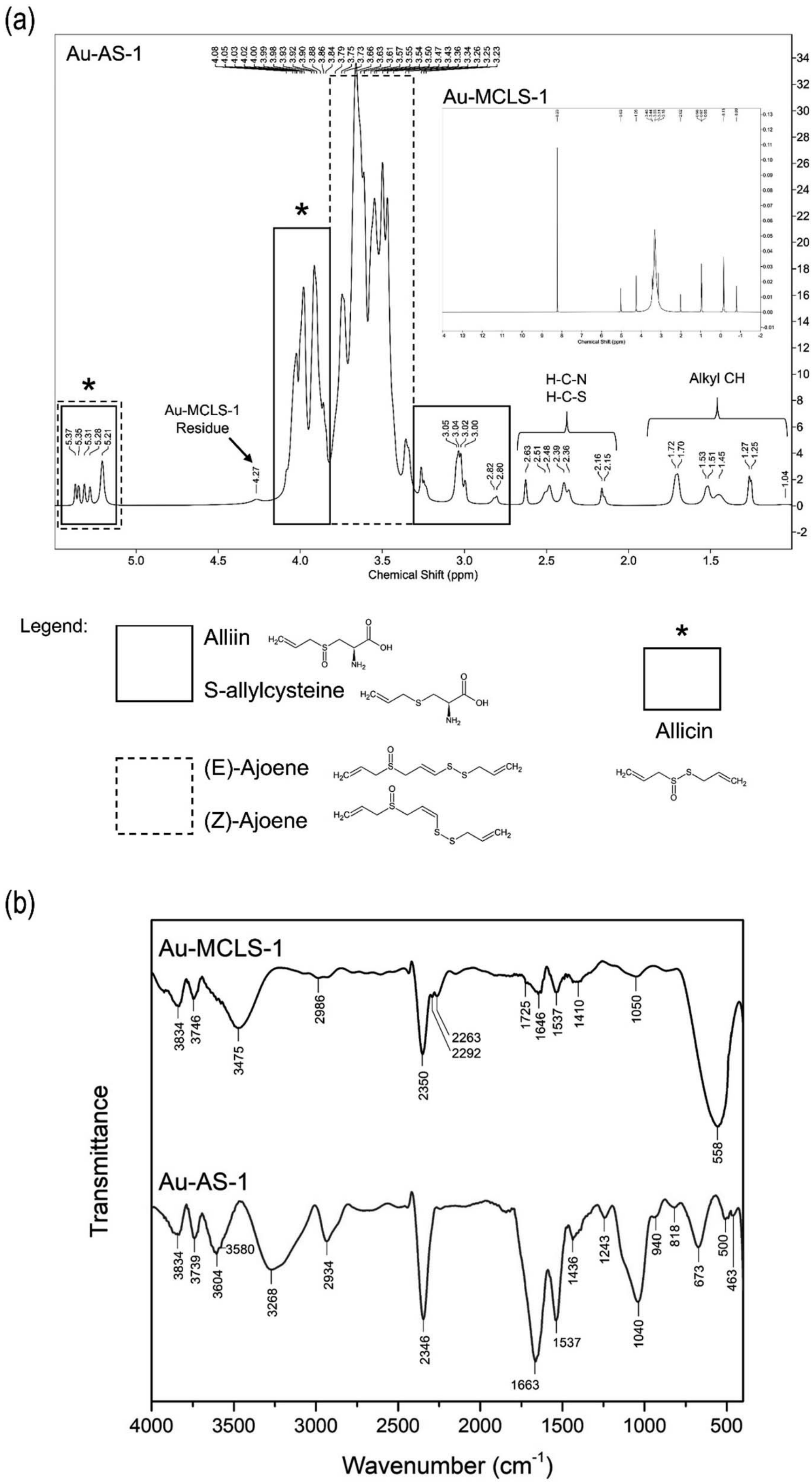

Fig. 6 Analysis and comparison of Au-MCLS-1 and Au-AS-1 compounds: (a) corresponding organosulfur compounds of AS extract obtained from ^{1}H NMR spectral features of Au-AS-1 nanoparticle system in comparison to the ^{1}H NMR spectra of Au-MCLS-1 as inset, and (b) FTIR spectral peaks corresponding to functional groups of Au-MCLS-1 before and after functionalization with AS extract to produce Au-AS-1. Differences in peak positions and features imply functionalization *via* substitution/displacement from Au-MCLS-1 to Au-AS-1.

Au-AS-1. Table S4† summarizes the ^{1}H NMR peak differences between Au-MCLS-1 and Au-AS-1. Based on the comparison, almost complete conversion from Au-MCLS-1 to Au-AS-1 was achieved. This is due to their differences in peak positions in which only a minor peak with very faint signal was detected in Au-AS-1 which was considered to be a residue from Au-MCLS-1. This residual peak was attributed to hydrogen atoms attached to either a cyclic structure or to a carbon atom bonded to another R group of a cyclic structure as stated previously on the discussion based on Ahmed *et al.* (2015)[26] and Al-Majed *et al.* (2018).[27] This could be due to polycyclic organic acid compounds found in MC or LS. Aside from this peak, all other ^{1}H NMR peaks of Au-AS-1 were different from those of Au-MCLS-1.

IR transmittance identify important functional groups of the organosulfur capping compounds. Additional information regarding the assessment of the viability of transforming Au-MCLS-1 to Au-AS-1 was also shown. The FTIR spectra comparison of Au-MCLS-1 an Au-AS-1 are shown in Fig. 6b. Both Au-MCLS-1 and Au-AS-1 have peaks at 3834 and 1537 cm^{-1} which were designated to the stretching of free hydroxyl which could be from phenolic structures and to the deformation of –NH, respectively. These peaks were considered as residual peaks from the capping compounds of Au-MCLS-1. Previously, a residual peak in ^{1}H NMR was due to hydrogen atoms attached to either a cyclic structure or to a carbon atom bonded to another *R* group of a cyclic structure. In the employed ^{1}H NMR spectroscopy, hydroxyl and –NH groups become undetected since deuterium from the deuterated water solvent exchanges with the hydrogen atoms of the hydroxyl and –NH groups. The hydrogens in NH, OH, COOH, and NH_2 groups, and those bonded to S atoms are exchangeable by deuterium.[39] By connecting the information from both analyses, it could be determined that the residual capping compounds from Au-MCLS-1 could be phenolic molecules having cyclic and amine groups in their structure or other similar derivatives. The FTIR peak of both Au-MCLS-1 and Au-AS-1 at 3834 cm^{-1} were of similar weak intensity, while in the ^{1}H NMR spectra, the peak at 4.26–4.27 ppm was extremely weak for Au-AS-1 as compared to Au-MCLS-1. However, the 1537 cm^{-1} peak from Au-MCLS-1 was of a significantly less degree as compared to that of Au-AS-1. Since two identified organosulfur compounds, alliin and *S*-allylcysteine, also have –NH groups in their structures, the increase in peak intensity could be attributed to these compounds. In general, it could still be considered that almost complete substitution or displacement by organosulfur compounds occurred in the processing of Au-MCLS-1 to form Au-AS-1. This could be further validated since aside from the FTIR peaks at 3834 and 1537 cm^{-1}, no other peaks were the same for the two Au nanoparticle systems.

The peaks at 3739, 3604, 3580, and 2934 cm^{-1} were due to the stretching of the free hydroxyl which can be assigned to the carboxylic acid functional groups. In addition to these, the 1436 cm^{-1} was attributed to the C=O group in the carboxylic structure. Meanwhile, at the 3268 and 1243 cm^{-1} peaks, the stretching of N–H and the amine C–N bond can be assigned, respectively. These peaks representing the carboxylic acid and amine functional groups can be associated with the presence of alliin and *S*-allylcysteine as substituting capping compounds. The presence of other organosulfur compounds such as ajoene, which can have (*E*)- and (*Z*)-isomers, and allicin can be related to the peaks at 500 and 463 cm^{-1} which are designated to the S–S bond. The S=O stretching at 1040 cm^{-1} can be attributed to alliin, allicin, and the two isomers of ajoene. The stretching of alkenyl C=C was assigned to the peak at 1663 cm^{-1} and the out-of-plane bending of alkene C–H was ascribed to the 940 cm^{-1} peak. Both the peaks at 818 and 673 cm^{-1} were due to the C–S bond stretching. The alkenyl C=C, alkene C–H, and C–S bonds are all characteristic features that are found in the structures of alliin, *S*-allylcysteine, (*E*)-ajoene, (*Z*)-ajoene, and allicin. Similar with all of the other Au nanoparticle systems investigated *via* FTIR analysis, Au-AS-1 also exhibited carbon dioxide adsorption capability as indicated by the peak at 2346 cm^{-1} which represents its asymmetric stretching. The comparison of the functional group summaries of Au-MCLS-1 and Au-AS-1 as determined by FTIR analysis are presented in Table S5.†

TEM with SAED of Au-AS-1 nanoparticle system. The TEM image of Au-AS-1 is shown in Fig. 7. Quasi-spherical nanoparticles are evident along with triangular and rod-shaped particles. These nanoparticle shapes were also observed in the SEM images of Au-MCLS-1 in the previous discussions. The rings on the diffraction pattern correspond to the (002), (022), (113), and (004) reflections of the structure of Au which is face-centered-cubic.

Au-AS-1 nanoparticle system stability. The stability of functionalized Au nanoparticle system from Au-MCLS-1 to Au-AS-1 was tested from its absorbance spectra at the start and end of a two-week period in dark storage conditions at about 4 °C. Ultrapure water was used as the dispersion medium of Au-AS-1 nanoparticles. The spectral comparison is presented in Fig. 8a. Similar to Au-MCLS-1 as previously discussed, there is no apparent change in the spectra of Au-AS-1 after the time of investigation. Hence, Au-AS-1 can also be considered as stable for two weeks. Moreover, the measured Au-AS-1 zeta potential (−19.6 mV) after five months as shown in Fig. 8b was less than that of Au-MCLS-1 (−21.3 mV). Yet, the values can still be comparable. Organosulfur compounds from AS extract can provide stabilization to Au nanoparticles.[40] Specifically, the observed stability could be imparted by the organosulfur compounds that substituted or displaced the previous capping compounds (*i.e.* oxidized polyphenols and organic acids). These organosulfur compounds such as alliin, *S*-allylcysteine, (*E*)-ajoene, (*Z*)-ajoene, and allicin could have acted as both capping and stabilizing compounds for the Au nanoparticles.

Displacement mechanism by organosulfur compounds. Organo-sulfur molecules could have superior chemisorption capability on the surface of Au.[41,42] It can be considered that the affinity of the oxidized polyphenols and organic acids on the surface of the Au nanoparticles is of a lesser degree than that of the AS compounds containing sulfur in their structures. Various organosulfur compounds are able to displace residues on the surface of Au nanoparticles, such as citrate-residues.[43] As the organosulfur compounds interact with the Au nanoparticles, the attractive forces become stronger for them to the point that

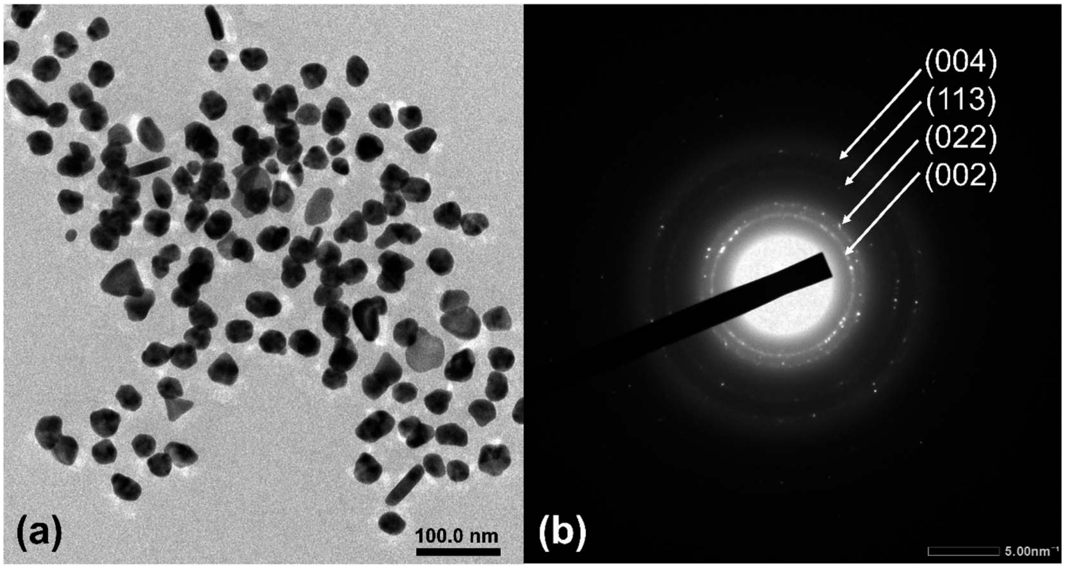

Fig. 7 Quasi-spherical, triangular, and rod-shaped nanoparticles are seen on the (a) TEM image of Au-AS-1, and (b) the (002), (022), (113), and (004) reflections of Au are shown *via* electron diffraction.

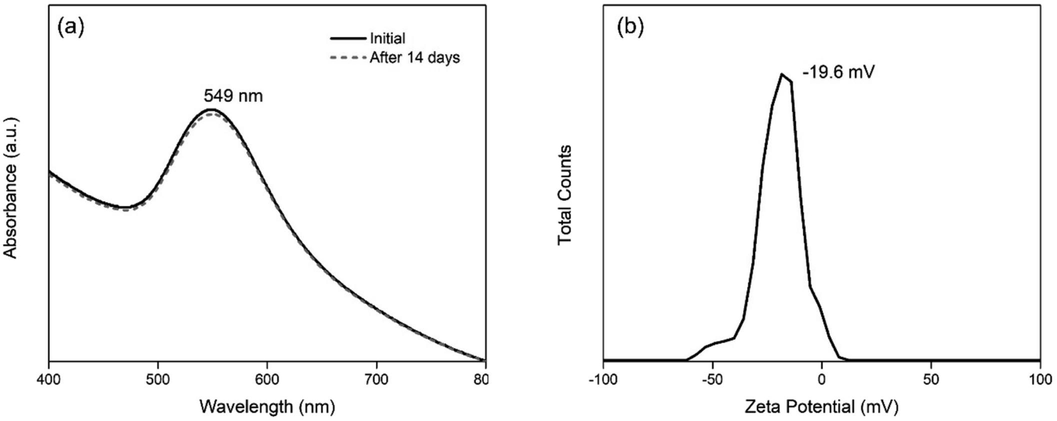

Fig. 8 Stability of Au-AS-1 nanoparticle system as shown by its (a) absorbance spectra over a two-week period, and (b) zeta potential value after five months.

their affinity is preferred over the affinity of oxidized polyphenols and organic acids. This situation triggers the detachment of the previous capping agents of Au-MCLS-1 and is eventually replaced by sulfur-containing compounds such as alliin, ajoene, *S*-allylcysteine, and allicin. The displacement/substitution of Au-MCLS-1 capping compounds by the organosulfur compounds of AS extract is illustrated in Fig. 9.

Au nanoparticle and ion interaction experiments

LSPR behavior with varying lead(II) ion concentrations. The detection of Pb^{2+} by Au-MCLS-1 nanoparticle system can be physically observed by the decrease of pinkish purple colloidal coloration intensity after the addition of ions as shown in Fig. S6a.† However, there is a difficulty in assigning a specific color tint to the Pb^{2+} concentration with which the Au-MCLS-1 nanoparticle system is exposed with. This limits the detection to qualitative means *via* naked-eye observation in which the presence, but not the quantity, of Pb^{2+} can be determined.

The interaction between Au-MCLS-1 nanoparticles and Pb^{2+} can be described by two distinct regions of their LSPR peak shift (nm) *versus* concentration (μM) plot as shown in Fig. 10a. The first region (0–283.78 μM) exhibits a linearly increasing relationship of Pb^{2+} concentration with LSPR peak shift. Meanwhile, the second region (283–851 μM) shows a quasi-plateau trend with fluctuations between Pb^{2+} concentrations with LSPR peak wavelength. The quasi-plateau trend could signify that the excess of Pb^{2+} does not significantly contribute to the LSPR peak shift of Au-MCLS-1, which could be attributed to the saturation of available hydroxyl functional groups that supposedly interact with the ions within the 283–851 μM range. In addition, the observed decrease of the absorbance with accompanying redshifting of the plasmon band could be

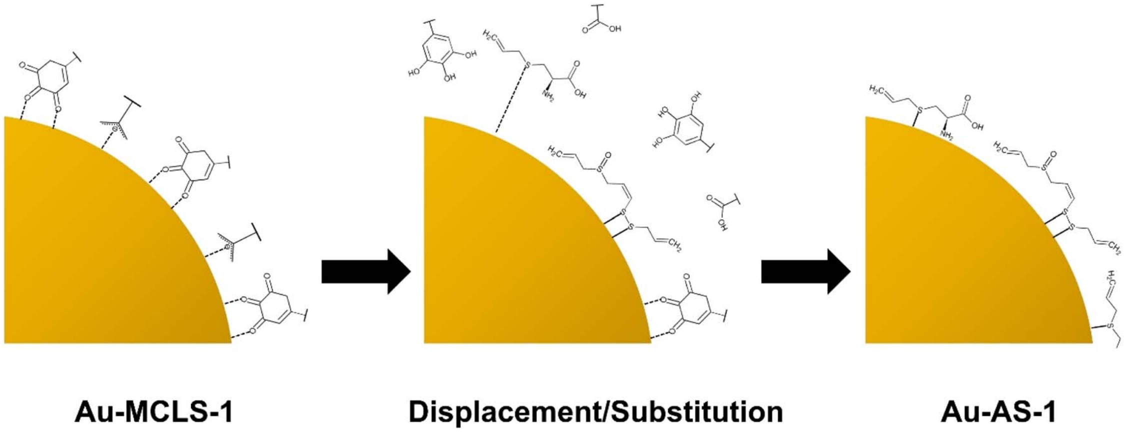

Fig. 9 Graphical representation of the displacement/substitution of Au-MCLS-1 capping compounds by alliin, SAC, (*E*)-ajoene, (*Z*)-ajoene, and allicin (not drawn to scale) showing the preference of Au to bind with S.

attributed to the nanoparticle aggregation as caused by increasing Pb^{2+} concentrations.[44,45]

The linear region (Fig. 10) is used to identify the Pb^{2+}-containing AuNP solution. However, the Pb^{2+} quantification would require at least a UV-vis spectrophotometer to measure peak shifts since color tint variations are not easily distinguishable visually.

Similar to Au-MCLS-1, the detection of Pb^{2+} by Au-AS-1 nanoparticle system can be observed from the reduction of violet colloidal coloration intensity after the addition of ions as shown in Fig. S6b.† However, similarly, associating a specific color tint to the Pb^{2+} concentration with which the Au-AS-1 nanoparticle system is exposed with is difficult. Due to this, only the presence, but not the quantity, of Pb^{2+} can be determined *via* naked-eye observation.

There are also two distinct regions for the LSPR peak shift (nm) *versus* concentration (μM) plot (Fig. 10b) of the interaction between Au-AS-1 nanoparticles and Pb^{2+}: linearly increasing

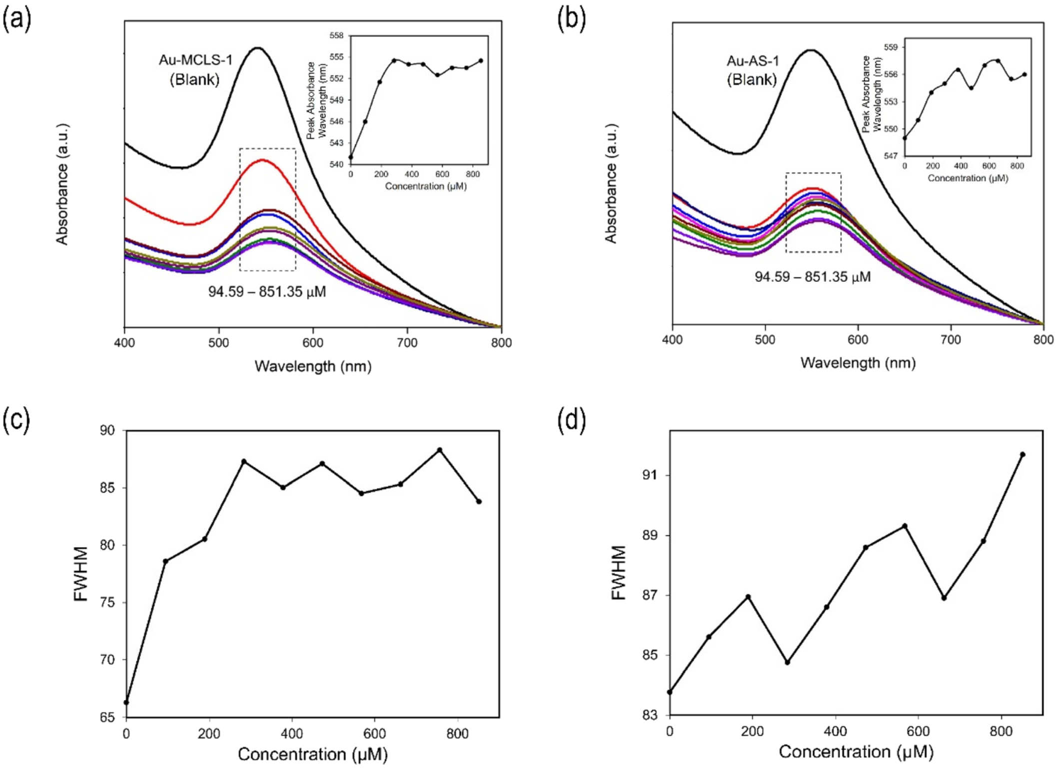

Fig. 10 Absorbance of (a) Au-MCLS-1 and (b) Au-AS-1 with varying Pb^{2+} concentrations and their corresponding plot of absorbance peak wavelength *vs.* concentration as inset. Full width at half maximum (FWHM) values of the absorbance spectra of (c) Au-MCLS-1 show a linearly increasing then a fluctuating trend with Pb^{2+}, while those of (d) Au-AS-1 indicate a fluctuating and generally increasing trend with Pb^{2+}. The FWHM values were obtained using the Origin software *via* Gaussian fitting.

behavior (0–378 μM) and fluctuating trend (378–851 μM). The peak shifts caused by Pb^{2+} are also accompanied by absorbance suppression which is in accordance to the observed decrease in colloidal color intensity. The region where linearity between LSPR peak shift and Pb^{2+} concentration exists can be used to determine the quantity of exposed ions with the Au-AS-1 nanoparticle system. This is because within the linear region, specific LSPR peak shifts can correspond to certain Pb^{2+} concentrations. However, with this method of ion quantification, a UV-vis spectrophotometer would be a requisite in order to determine peak shifts since colloidal color tint differences are difficult to observe *via* naked-eye means.

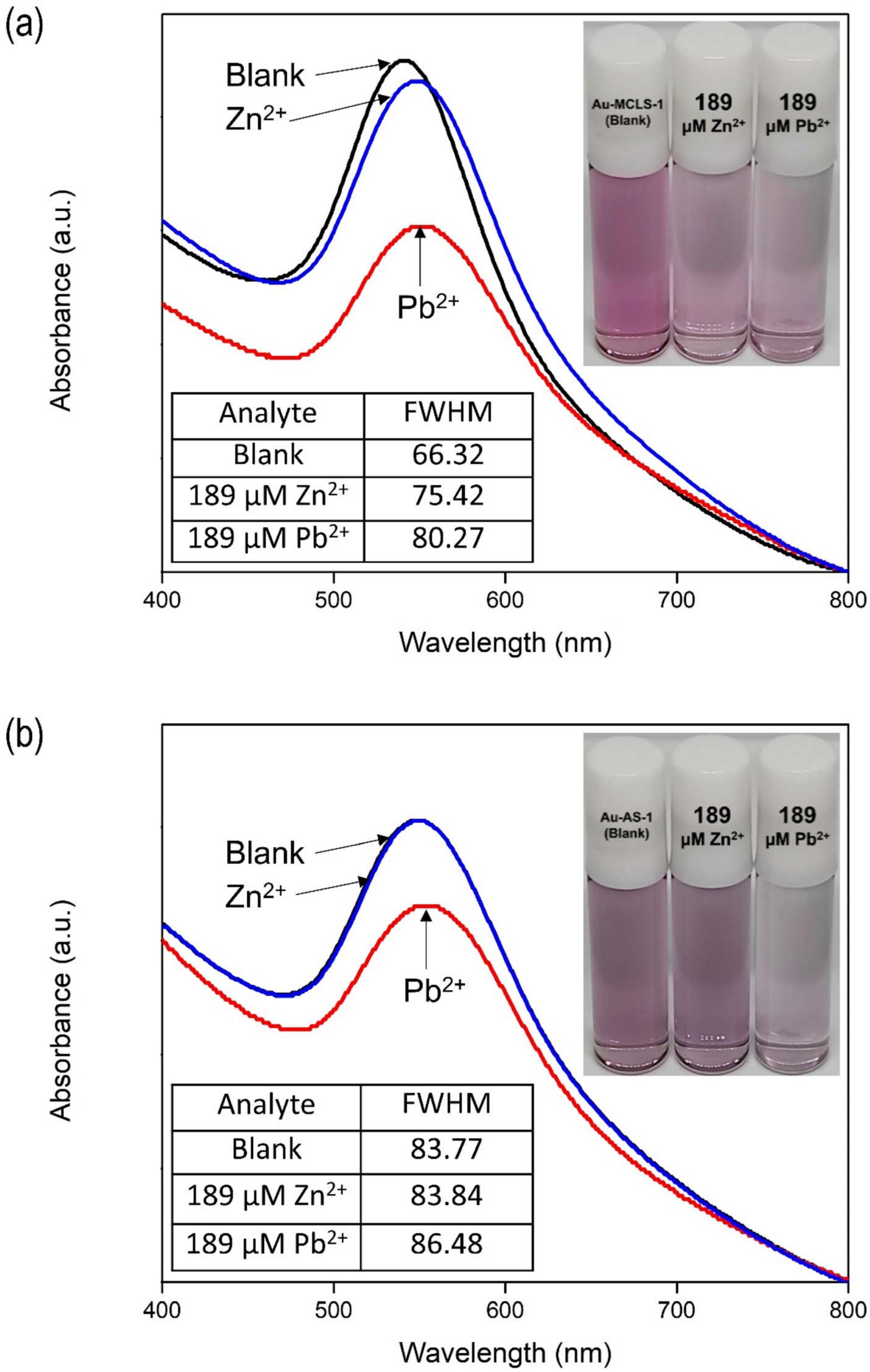

(a)

Analyte	FWHM
Blank	66.32
189 μM Zn^{2+}	75.42
189 μM Pb^{2+}	80.27

(b)

Analyte	FWHM
Blank	83.77
189 μM Zn^{2+}	83.84
189 μM Pb^{2+}	86.48

Fig. 11 Absorbance spectra and color comparisons of (a) Au-MCLS-1 and (b) Au-AS-1 nanoparticle systems upon exposure to ultrapure water and 189 μM Pb^{2+} or Zn^{2+}. FWHM values of the absorbance of Au-MCLS-1 increased due to Pb^{2+} and Zn^{2+}. FWHM of the absorbance of Au-AS-1 increased due to Pb^{2+} while the change due to Zn^{2+} can be considered insignificant. Au-AS-1 is more selective to Pb^{2+} than Zn^{2+} as compared to Au-MCLS-1. The FWHM values were obtained using the Origin software *via* Gaussian fitting.

In general, minimal shifting of LSPR peaks were observed in the experiments. These minimal changes can be due to the ion concentrations which were not high enough to cause drastic shifts or even immediate aggregations. Further increasing the concentrations, may give rise to larger shifts and/or separate peaks due to aggregations.

LSPR behavior with lead(II) versus zinc ions. The zinc ion (Zn^{2+}) interaction experiment served as a reference of comparison with Pb^{2+}. After the addition of Pb^{2+} or Zn^{2+}, Au-MCLS-1 nanoparticle system color intensity was lower compared to addition of blank. Au-MCLS-1 nanoparticles both responded to Pb^{2+} or Zn^{2+} in terms of LSPR shift as determined by absorbance spectroscopy in Fig. 11a. However, the peak shift was redder in Pb^{2+} as compared to Zn^{2+}. The shift of LSPR peak to the red and decrease in intensity was seen to a lesser extent in Zn^{2+}-containing solution that in Pb^{2+}. It showed that Au-MCLS-1 does not have good differentiation between these two divalent ions. Hence, the Au-MCLS-1 nanoparticle system can either be used to detect Pb^{2+} or Zn^{2+} in separate systems.

The addition of Zn^{2+} to Au-AS-1 did not change the colloidal color, while Pb^{2+} exposure reduced the intensity. The LSPR of Au-AS-1 nanoparticles shifted significantly upon the exposure to Pb^{2+}, while very minimal or negligible change was observed in its absorbance spectrum after Zn^{2+} were introduced into the system as shown in Fig. 11b. This means that the Au-AS-1 nanoparticle can differentiate between Pb^{2+} and Zn^{2+}.

The decrease in observed intensity can also be explained in terms of the Pb^{2+}- and Zn^{2+}-induced destabilization of Au-MCLS-1 nanoparticles, and Pb^{2+}-induced destabilization of Au-AS-1 nanoparticles, wherein the net negative charge on the surface of nanoparticles are destabilized.[46,47] The ions cause the destabilization or particle aggregation that manifests as absorption peak broadening accompanied by redshifting. Initial response of the Au nanoparticle systems is decrease in bulk color intensity attributed to agglomeration due to the attractive forces caused by either or both ions to the capping compounds of Au nanoparticles. When the nanoparticles form networks, the absorption peak of the colloidal system becomes less pronounced. Meanwhile, after prolonged periods of time, the Pb^{2+}-spiked colloidal systems and Zn^{2+}-spiked Au-MCLS-1 system become clear with suspended dark violet to blackish aggregated particles.

Mechanism of lead(II) and zinc(II) ion interaction with Au nanoparticles. The mechanism of detection is due to the ion-induced attractive forces among Au nanoparticles within the colloidal system as highlighted in the graphical representations in Fig. 12 as based on previous studies.[44,48–51] As shown, both Pb^{2+} and Zn^{2+} decrease the interparticle distances of Au-MCLS-1 nanoparticles wherein Pb^{2+} effects are more pronounced as compared to Zn^{2+}. Meanwhile, Pb^{2+} reduce the interparticle distances of Au-AS-1 nanoparticles, but the presence of Zn^{2+} have no significant effect on the particle separation. The capping compounds of the nanoparticles are also responsible for the interactions since they tend to be attracted to the ions. Specifically, carboxylic acid functional groups in the capping compounds of Au-MCLS-1 and Au-AS-1

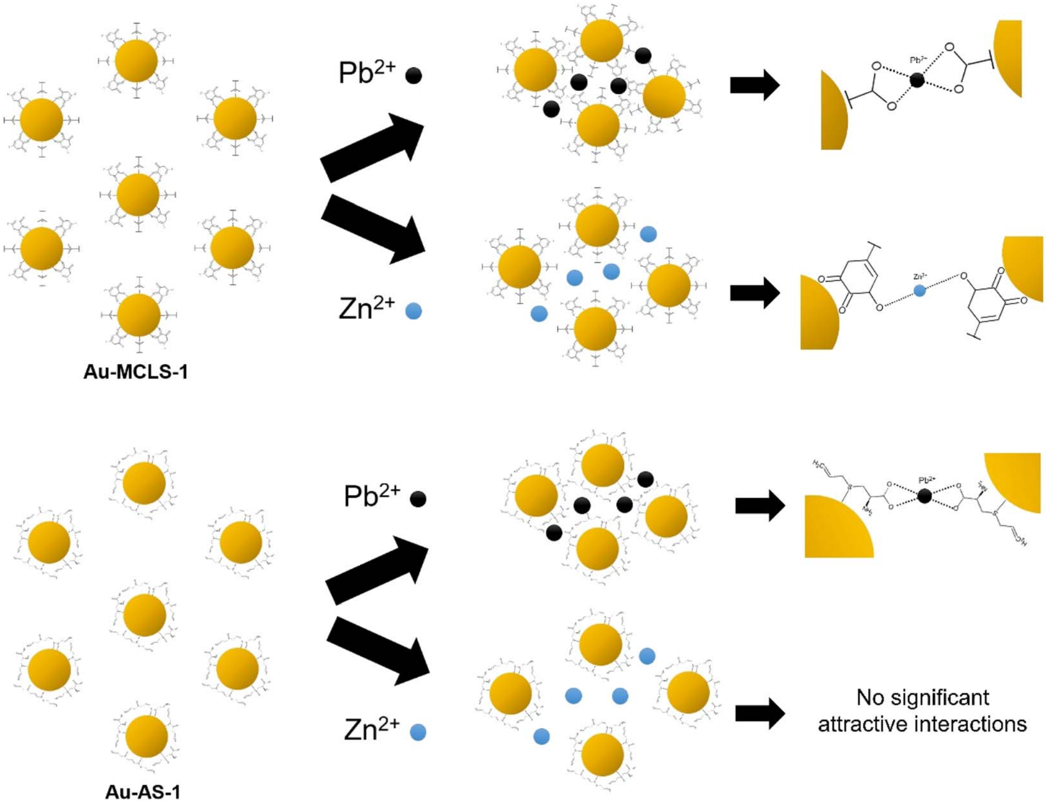

Fig. 12 Graphical representation of the effects of Pb^{2+} or Zn^{2+} on the interparticle distances of Au-MCLS-1 and Au-AS-1 nanoparticles (not drawn to scale). Au-AS-1 has more selectivity to Pb^{2+} as compared to Au-MCLS-1 due to the selective affinity of capping compounds.[44,48–51]

make them capable of attractive interactions with Pb^{2+}. The carboxylic acid functional group, however, does not have an affinity with Zn^{2+} that is why Au-AS-1 is selective to Pb^{2+}. Similar observations were previously reported in which the carboxylic acid/carboxylate group exhibited a strong affinity and high selectivity to Pb^{2+} as compared to other ions such as Zn^{2+}.[47,48,51] In the case of Au-MCLS-1 nanoparticles which did not exhibit ion selectivity, other capping compounds such as polyphenols tend to chelate Zn^{2+}.[49,50] As the attraction between the ions and capped Au nanoparticles becomes

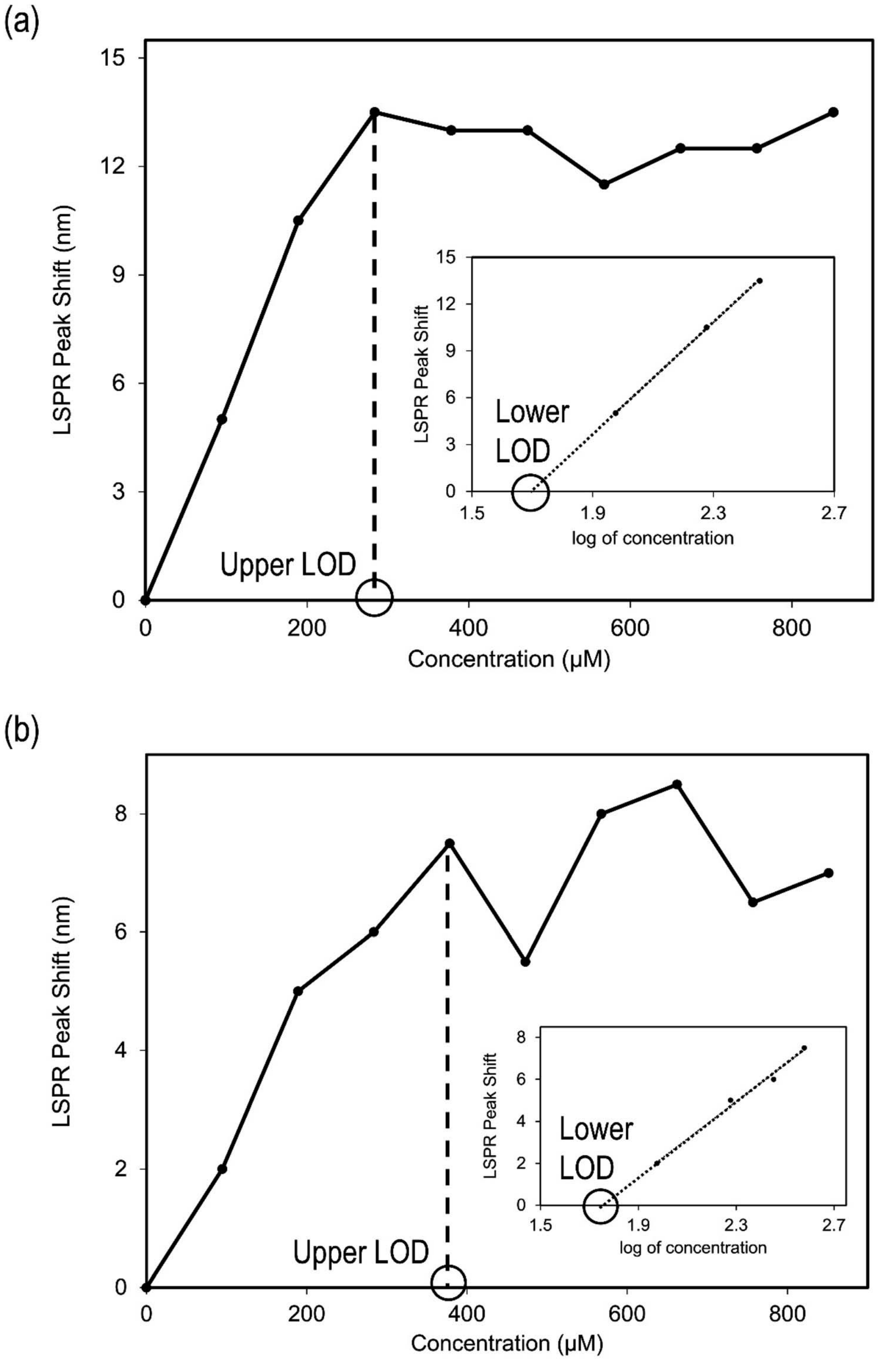

Fig. 13 Plots of peak shift *vs.* concentration and linear regression analysis of shift in peak *vs.* log concentration plots for (a) Au-MCLS-1: upper LOD is 284 μM (59 ppm) and the lower LOD is 49 μM (10 ppm), and (b) Au-AS-1: upper LOD is 378 μM (78 ppm) and the lower LOD is 55 μM (11 ppm).

dominant, interparticle distances become less and the particles could reach a point of aggregation. Ion-chelation interactions lead to the destabilization of the net negative charge on the surface of the nanoparticles which result to nanoparticle aggregation, and can be observed as LSPR band intensity reduction with redshift.[44–47,52] Further aggregation after prolonged periods of time or exposure to very high ion concentration could cause the system to be clear due to the coagulation of the nanoparticles in which dispersion becomes hindered.

The degree of aggregation can be dependent on the concentration of ions. As previously discussed, there are certain concentration ranges wherein the LSPR peak shift has linear relationship with Pb^{2+} concentration. These ranges could be exploited for the quantification of ions. Above these concentration ranges, erratic fluctuations in detection could occur. But even if ion quantification is not possible for the fluctuating regions, qualitative ion detection could still be done: Au-MCLS-1 could be used for confirming the presence of Pb^{2+} and/or Zn^{2+}, then Au-AS-1 can be used to selectively confirm Pb^{2+} presence.

Determination of upper and lower limits of lead(II) ion detection. The upper limit of detection (LOD) was designated as the highest Pb^{2+} concentration in which an increasing linear relationship between wavelength and concentration exists. It is important to note the upper LOD does not restrict the Au nanoparticle systems from being practicable to high concentrations of Pb^{2+}. High Pb^{2+} concentrations can still be qualitatively detected by the Au nanoparticle systems in which rapid particle coagulation occurs, making the medium clear. This manifestation could confirm the presence of high Pb^{2+} *via* naked-eye detection. However, ion quantification would not be applicable for this case. Quantification could only be done within the linear region in which specific LSPR shifts correspond to certain ion concentrations. The upper limits of detection for Au-MCLS-1 and Au-AS-1 are 283 μM (59 ppm) and 378 μM (78 ppm), respectively.

In order to determine the lower limits of detection of Au-MCLS-1 and Au-AS-1, linear regression analysis was performed on the LSPR peak shift *versus* log of Pb^{2+} concentration plots. The lower limits of detection are the extrapolated concentration values after obtaining the linear equations. These values correspond to the maximum Pb^{2+} concentration with which no LSPR peak shift is exhibited. The lower limits of detection for Au-MCLS-1 and Au-AS-1 are 49 μM (10 ppm) and 55 μM (11 ppm), respectively. Fig. 13a and b show the plot of peak shift *vs.* concentration and linear regression analysis of shift in peak *vs.* logarithm of concentration for Au-MCLS-1 and Au-AS-1, respectively. In comparison to literature, the lower limits of Pb^{2+} detection of Au-MCLS-1 (49.44 μM) and Au-AS-1 (55.18 μM) are significantly greater than that of the Au nanoparticles prepared in the study of Chai *et al.*[53] and Mao *et al.*,[54] having 0.1 μM of minimum detection limit. Despite this, the prepared Au nanoparticles could still be used in ion detection applications of relatively higher permissible limits of Pb^{2+}.

Ayers and Westcot (1985) recommended 5 ppm as the permissible amount of lead in irrigation water,[10] and this value was used by Farid *et al.* (2015)[11] as basis for assessing environmental waters. Although the lower limits of detection for Au-MCLS-1 (10.24 ppm) and Au-AS-1 (11.43 ppm) are above this value, the differences can still be considered as not too pronounced. Moreover, Au-MCLS-1 and Au-AS-1 nanoparticle systems could still be used for initial screening of water samples.

In addition, the Au-AS-1 nanoparticle system have the potential to be used for the assessment of environmental water remediation effectiveness especially in achieving Pb^{2+} concentrations below the severe effect level of 250 ppm as stated by NOAA.[12]

Conclusions

Stable and nearly-monodisperse Au nanoparticle systems were biosynthesized *via* a relatively rapid one-pot approach at room temperature with manual agitation using different combinations of leaf extracts (MCLS, LSMO, MCMO, and MLM), and functionalized using heat-treated AS cloves extract. The sizes of the quasi-spherical Au nanoparticles have significant differences among different combinations of leaf extracts. Organic acids and polyphenols from leaf extracts were found to be of major contribution to the Au nanoparticles' makeup. In the functionalization, almost complete displacement of Au-MCLS-1 capping and stabilizing compounds occurred due to substitution by the biochemical compounds from AS extract such as alliin, *S*-allylcysteine, allicin, and ajoene. The interaction of Au-MCLS-1 to Pb^{2+} is almost similar to its interaction with Zn^{2+}, while Au-AS-1 tends to be more selective to Pb^{2+} as compared to Zn^{2+}. Based on the investigations, the highlighted straightforward biosynthesis and functionalization methods are viable for Au nanoparticle system processing, and the Au-MCLS-1 and Au-AS-1 nanoparticle systems have the potential to be used in the detection of divalent ions (*i.e.* Pb^{2+} or Zn^{2+}) and Pb^{2+}, respectively.

Conflicts of interest

There are no conflicts to declare.

Acknowledgements

The authors thank the Department of Science and Technology – Science Education Institute and Engineering Research and Development for Technology for the funding.

References

1 V. Dhumale, R. Gangwar and N. Pande, *Mater. Res. Innovations*, 2020, **25**, 354–362.

2 K. Parveen, V. Banse and L. Ledwani, *AIP Conf. Proc.*, 2016, **1724**, 020048.

3 L. Bertel Garay, F. Martínez Ortega and S. Méndez-Sanchez, *J. Mex. Chem. Soc.*, 2018, **62**, 1–9.

4 J. Wai and S. New, *RSC Adv.*, 2020, **10**, 1088–1094.

5 N. Komova, K. Serebrennikova, A. Berlina, S. Pridvorova, A. Zherdev and B. Dzantiev, *The 1st International Electronic Conference on Chemical Sensors and Analytical Chemistry*, 2021, 5, p. 6.
6 M. Balali-Mood, K. Naseri, Z. Tahergorabi, M. Khazdair and M. Sadeghi, *Front. Pharmacol.*, 2021, **12**, 1–19.
7 P. Tchounwou, C. Yedjou, A. Patlolla and D. Sutton, *Exper. Suppl.*, 2012, 133–164.
8 U.S. Environmental Protection Agency, *Lead and Copper Rule*, **https://www.epa.gov/dwreginfo/lead-and-copper-rule#:~:text=The1991Rule,-In1991%2CEPA&text=Theruleestablishedamaximum,copperwithinthedistributionsystem**, (accessed May 2022).
9 U.S. Environmental Protection Agency, *Lead and Copper Rule: Summary of Revisions*, **http://nepis.epa.gov/Exe/ZyPDF.cgi?Dockey=P1005884.txt**, (accessed May 2022).
10 R. Ayers and D. Westcot, *Water quality for agriculture*, Food and Agriculture Organization, Rome, 1985.
11 G. Farid, N. Sarwar, Saifullah, A. Ahmad, A. Ghafoor and M. Rehman, *Adv. Crop Sci. Technol.*, 2015, **4**, 1–7.
12 National Oceanic and Atmospheric Administration, *Screening Quick Reference Tables*, **https://response.restoration.noaa.gov/sites/default/files/SQuiRTs.pdf**, (accessed May 2022).
13 J. Anderson, E. Bowden and P. Pickup, *Anal. Chem.*, 1996, **68**, 379R–444R.
14 A. Burlingame, R. Boyd and S. Gaskell, *Anal. Chem.*, 1996, 599R–651R.
15 K. Jackson and G. Chen, *Anal. Chem.*, 1996, **68**, 231R–256R.
16 T. Lin and M. Chung, *Sensors*, 2008, **8**, 582–593.
17 K. Yoosaf, B. Ipe, C. Suresh and K. Thomas, *J. Phys. Chem. C*, 2007, **111**, 12839–12847.
18 M. McDonald, I. Mila and A. Scalbert, *J. Agric. Food Chem.*, 1996, **44**, 599–606.
19 N. Modi, T. Goel, T. Das, S. Malik, S. Suri, A. Rawat, S. Srivastava, R. Tuli, S. Malhotra and S. Gupta, *Indian J. Med. Res.*, 2013, **137**, 540–548.
20 G. Oboh, A. Ademiluyi, A. Ademosun, T. Olasehinde, S. Oyeleye, A. Boligon and M. Athayde, *Biochem. Res. Int.*, 2015, 1–8.
21 Z. Zakaria, N. Mahmood, S. Mamat, N. Nasir and M. Omar, *Front. Pharmacol.*, 2018, **8**, 982.
22 S. Santhosha, P. Jamuna and S. Prabhavathi, *Food Biosci.*, 2013, **3**, 59–74.
23 J. Imai, N. Ide, S. Nagae, T. Moriguchi, H. Matsuura and Y. Itakura, *Planta Med.*, 1994, **60**, 417–420.
24 F. Rajathi, R. Arumugam, S. Saravanan and P. Anantharaman, *J. Photochem. Photobiol., Bc*, 2014, **135**, 75–80.
25 G. Wang and W. Sun, *J. Phys. Chem. B*, 2006, **110**, 20901–20905.
26 Y. Ahmed, Z. Yaakob, P. Akhtar, M. Rahman and F. Islam, *Int. J. Pharmacol.*, 2015, **11**, 821–827.
27 A. Al-Majed, A. Bakheit, R. Alharbi and H. Abdel Aziz, *Profiles of Drug Substances, Excipients and Related Methodology*, 2018, pp. 209–254.
28 N. Bai, K. He, M. Roller, B. Zheng, X. Chen, Z. Shao, T. Peng and Q. Zheng, *J. Agric. Food Chem.*, 2008, **56**, 11668–11674.
29 M. Vergara-Jimenez, M. Almatrafi and M. Fernandez, *Antioxidants*, 2017, **6**, 91.
30 S. Dash, R. Majumdar, A. Sikder, B. Bag and B. Patra, *Appl. Nanosci.*, 2014, **4**, 485–490.
31 K. Kumar, B. Mandal, H. Kiran Kumar and S. Maddinedi, *Spectrochim. Acta, Part A*, 2013, **116**, 539–545.
32 H. Liu, X. Zhang, Z. Xu, Y. Wang, Y. Ke, Z. Jiang, Z. Yuan and H. Li, *Nanotechnology*, 2020, **31**, 415601.
33 S. Moreno-Álvarez, G. Martínez-Castañón, N. Niño-Martínez, J. Reyes-Macias, N. Patiño-Marin, J. Loyola-Rodriguez and F. Ruiz, *J. Nanopart. Res.*, 2010, **12**, 2741–2746.
34 M. Ouellette, F. Masse, M. Lefebvre-Demers, Q. Maestracci, P. Grenier, R. Millar, N. Bertrand, M. Prieto and E. Boisselier, *Sci. Rep.*, 2018, **8**, 14357.
35 L. Jayathilaka, S. Gupta, J. Huang, J. Lee and B. Lee, *J. Biomol. Tech.*, 2014.
36 J. Debouzy, J. Neumann, M. Hervé, D. Daveloose, J. Viret and R. Apitz-Castro, *Eur. Biophys. J.*, 1989, **17**, 211–216.
37 L. Small, J. Bailey and C. Cavallito, *J. Am. Chem. Soc.*, 1947, **69**, 1710–1713.
38 A. Roseblade, A. Ung and M. Bebawy, *Acta Pharmacol. Sin.*, 2017, **38**, 1353–1368.
39 G. Chen, I. Daaro, B. Pramanik and J. Piwinski, *J. Mass Spectrom.*, 2009, **44**, 203–213.
40 Y. Yulizar, H. Ariyanta and L. Abduracman, *Bull. Chem. React. Eng. Catal.*, 2017, **12**, 212–218.
41 L. Yang, X. Zhang, J. Wang, H. Sun and L. Jiang, *Microchim. Acta*, 2018, **185**, 472.
42 R. Nuzzo, B. Zegarski and L. Dubois, *J. Am. Chem. Soc.*, 1987, **109**, 733–740.
43 G. Perera, S. Athukorale, F. Perez, C. Pittman, Jr and D. Zhang, *J. Colloid Interface Sci.*, 2017, **511**, 335–343.
44 V. Le, T. Duong, V. Le, T. Phan, T. Nguyen, T. Chau and V. Doan, *RSC Adv.*, 2021, **11**, 15438–15448.
45 T. Mostowtt, J. Munoz and B. McCord, *The Analyst*, 2019, **144**, 6404–6414.
46 M. Annadhasan, T. Muthukumarasamyvel, V. R. Sankar Babu and N. Rajendiran, *ACS Sustainable Chem. Eng.*, 2014, **2**, 887–896.
47 E. Priyadarshini and N. Pradhan, *Sci. Rep.*, 2017, **7**, 1–8.
48 N. Ratnarathorn, O. Chailapakul and W. Dungchai, *Talanta*, 2015, **132**, 613–618.
49 K. Filipiak, M. Hidalgo, J. Silvan, B. Fabre, R. Carbajo, A. Pineda-Lucena, A. Ramos, B. de Pascual-Teresa and S. de Pascual-Teresa, *Food Funct.*, 2014, **5**, 381–389.
50 J. Pang, J. Yen, H. Wu and S. Huang, *Int. J. Mol. Sci.*, 2017, **18**, 1354.
51 Y. Kim, R. C. Johnson and J. T. Hupp, *Nano Lett.*, 2001, **1**, 165–167.
52 L. Chen, J. Li and L. Chen, *ACS Appl. Mater. Interfaces*, 2014, **6**, 15897–15904.
53 F. Chai, C. Wang, T. Wang, L. Li and Z. Su, *ACS Appl. Mater. Interfaces*, 2010, **2**, 1466–1470.
54 X. Mao, Z.-P. Li and Z.-Y. Tang, *Front. Mater. Sci.*, 2010, **5**, 322–328.